

Article

Optimization of Shape-Variable Gamma Camera to High-Dose-Rate Regions

Kengo Miyada ^{1,†}, Eiji Takada ^{2,*} and Yuki Sato ³

¹ ECODesign Engineering Program, National Institute of Technology (KOSEN), Toyama College, 13 Hongo-machi, Toyama 939-8630, Japan

² Headquarter, National Institute of Technology (KOSEN), Gakujutsu-Sogo-Center 10F, Hitotsubashi 2-1-2, Chiyoda-ku 101-0003, Japan

³ Collaborative Laboratories for Advanced Decommissioning Science, Japan Atomic Energy Agency, 790-1 Ohtsuka, Fukushima 979-1151, Japan; sato.yuki@jaea.go.jp

* Correspondence: e_takada@kosen-k.go.jp

† Present address: Department of Quantum Science and Energy Engineering, Graduate School of Engineering, Tohoku University, Aobayama 6-6-01-2, Sendai 980-8579, Japan.

Abstract: To proceed with the decommissioning of the Fukushima Daiichi Nuclear Power Station, it is necessary to visualize radioactive substances using a gamma camera in high-dose-rate regions inside a nuclear reactor building. We developed an umbrella-shaped Compton camera, whose sensitivity distribution can be adjusted by changing its shape. When used on a robot, the moving distance of the robot can be reduced compared to a pinhole camera that is sensitive only to the front surface. In addition, unlike an omnidirectional Compton camera, the sensitivity in a specific direction can be increased, which is expected to expand the degree of freedom of measurement. In this study, the characteristics of the developed system were evaluated through simulations and experiments for application in a high-level radioactive environment inside a reactor building. It is estimated that this system can operate at a dose rate of approximately 2.68 mSv/h. Furthermore, we devised a method to compensate for the effect of the dead time of the SiPM (MPPC) in the high-dose-rate region by monitoring the current of the SiPM drive power supply and evaluating its applicability to high dose rates. This correction method was validated in the case where the photoelectric peak of the energy spectra fluctuated by approximately 60 keV due to dead time.

Keywords: Compton camera; decommissioning; Ce:GAGG; SiPM (MPPC); EGS5



Citation: Miyada, K.; Takada, E.; Sato, Y. Optimization of Shape-Variable Gamma Camera to High-Dose-Rate Regions. *Electronics* **2023**, *12*, 2640. <https://doi.org/10.3390/electronics12122640>

Academic Editors: Gian-Franco Dalla Betta and Lodovico Ratti

Received: 11 April 2023

Revised: 8 June 2023

Accepted: 9 June 2023

Published: 12 June 2023



Copyright: © 2023 by the authors. Licensee MDPI, Basel, Switzerland. This article is an open access article distributed under the terms and conditions of the Creative Commons Attribution (CC BY) license (<https://creativecommons.org/licenses/by/4.0/>).

1. Introduction

Due to the tsunami caused by the Great East Japan Earthquake that occurred on March 11, 2011, several reactors at the Fukushima Daiichi Nuclear Power Station failed to cool their cores, and hydrogen explosions occurred in reactor buildings [1]. As a result, radioactive substances scattered inside and outside the power stations [2]. Therefore, in preparation for decommissioning measures, it is necessary to secure the work environment by visualizing and removing radioactive substances inside reactor buildings. For the visualization of these radioactive substances, a gamma camera, which can measure a wide range of contamination at once, is promising. To date, several studies on pinhole cameras [3–6] and Compton cameras [7,8] for the visualization of radioactive substances in nuclear reactor buildings have been carried out. Pinhole cameras tend to be large and heavy because they require extensive shielding, such as lead shielding; however, due to the simplicity of the principle and structure of the device, they offer high quantitative accuracy. On the other hand, Compton cameras require no shielding and are lightweight, which makes them easy to install on robots. Furthermore, by introducing shape variability in Compton cameras with an umbrella shape, the following advantages can be expected when installed on robots: (1) The moving distance of robots may be shortened when measuring the source intensity

distribution in each direction compared to a robot installed with a pinhole camera that is sensitive only to the front; (2) Unlike omnidirectional Compton cameras, the sensitivity distribution can be adjusted by changing the umbrella shape, thus expanding the degrees of freedom of measurement, such as by increasing the sensitivity in a specific direction. Therefore, as shown in Figure 1, we developed an umbrella-shaped Compton camera whose sensitivity distribution can be adjusted by changing its shape.

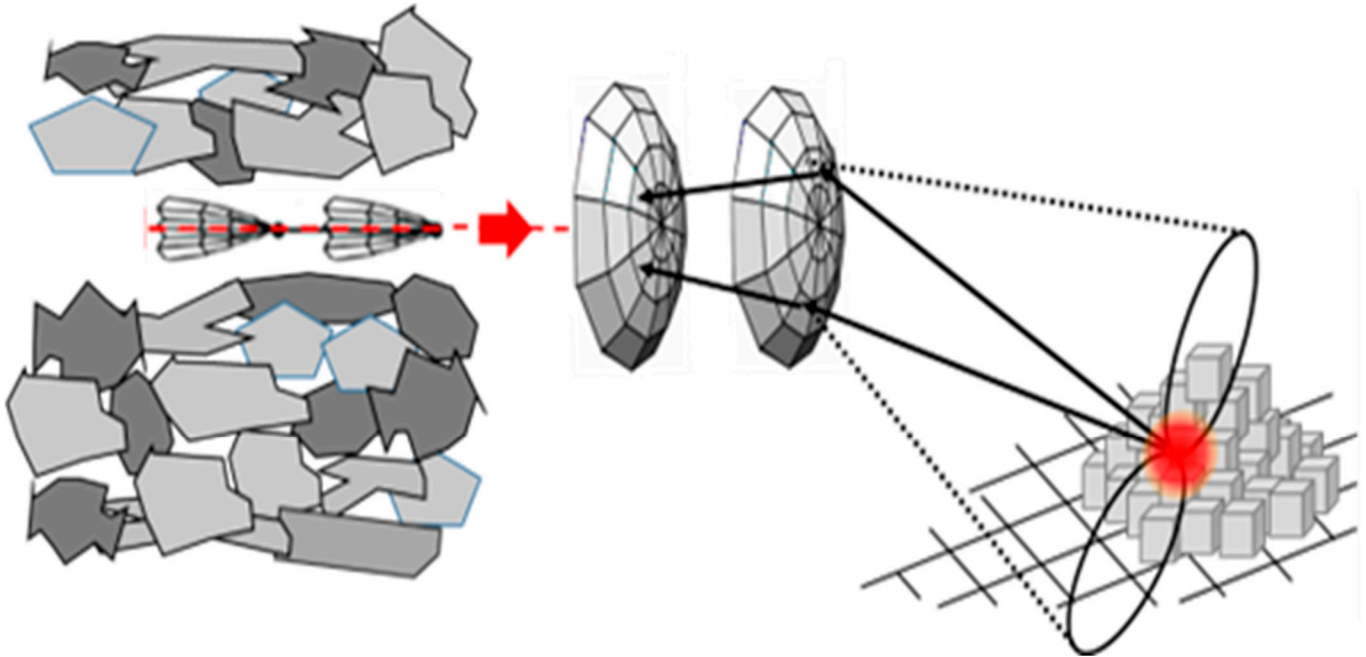


Figure 1. Image of the Compton camera in the nuclear setup. Changing shape is possible as shown by the red arrows.

In this study, the characteristics of the developed system were evaluated through simulations and experiments for application in a high-level radioactive environment inside a reactor building. The demand for gamma cameras that can operate at high dose rates is particularly high in the decommissioning work at the Fukushima Daiichi Nuclear Power Plant, and a report has been made of measurements inside the reactor building using a pinhole camera that visualized a hotspot in an environment of 659 mSv/h [4]. However, it weighs as much as 100 kg. On the other hand, Compton cameras can be constructed weighing only a few kgs, making them more suitable for use on robots than pinhole cameras. Measurements inside the turbine building using a Compton camera whose scintillator (Ce:GAGG) size is $1.5 \times 1.5 \times 5 \text{ mm}^3$ for the scatterer and $1.5 \times 1.5 \times 10 \text{ mm}^3$ for the absorber have successfully visualized a hotspot with a surface dose rate of up to 3.5 mSv/h in an environment of 0.4 to 0.5 mSv/h [9]. In addition, although the overall weight is 32.5 kg when shielded by a 45 mm thick lead, there is an example of application in an environment with an air dose rate of 40 to 60 mSv/h inside the reactor building [8]. In this study, the ultimate goal is to expand the applicable range of the system to about 100 mSv/h and to cover most regions inside the nuclear reactor building for measurement. We developed a Compton camera consisting of Ce:GAGG scintillators of $4 \times 4 \times 4 \text{ mm}^3$ size and the SiPMs, and evaluated the applicable dose rate, estimating that it can operate at dose rates above approximately 2.68 mSv/h without shielding. By reducing the scintillator size and providing shielding to the extent possible for mounting on a robot, it is expected that it can be applied to even higher dose rates. Furthermore, we devised a method to compensate for the effect of the dead time of the SiPM (MPPC) in the high-dose-rate region by monitoring the current of the SiPM drive power supply and evaluating the applicability of the system to high dose rates.

2. Compton Camera Overview

A Compton camera is a device that utilizes the phenomenon of gamma rays imparting energy to the detector through Compton scattering and photoelectric absorption to determine the direction of incident gamma rays [10]. As shown in Figure 2, the detector of a Compton camera is divided into a scatterer and an absorber and consists of two stages.

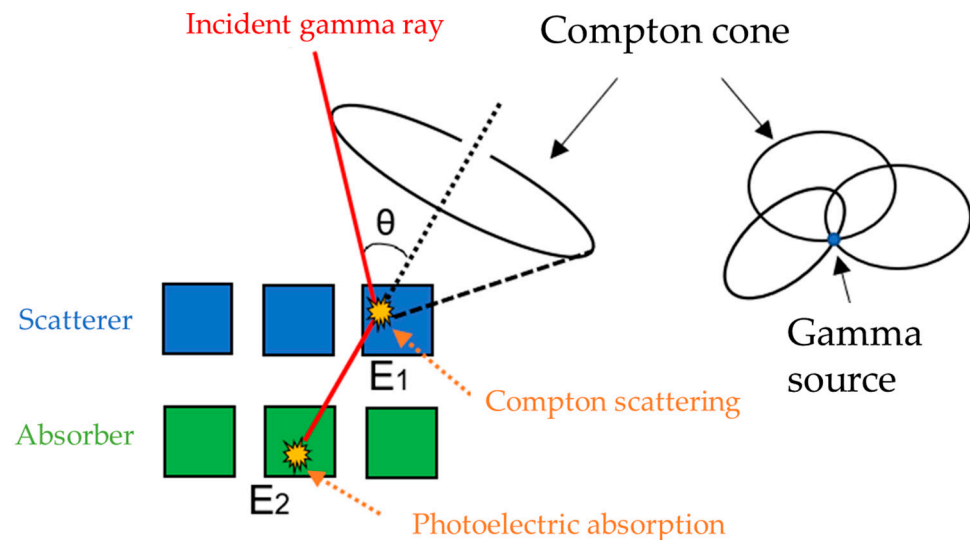


Figure 2. Working principle of Compton camera.

When the incident gamma ray is Compton-scattered by the scatterer, the scattered gamma rays impart some of their energy (E_1) to the scatterer and are scattered in the direction of angle θ (scattering angle). The scattered gamma rays then cause Compton scattering or photoelectric absorption in the absorber, thereby imparting the energy (E_2) to the absorber. A conical surface (Compton cone) is drawn to estimate the direction in which the incident gamma ray flows from the information of θ obtained from Equation (1), using the position information of the scatterer and absorber to which the incident gamma ray imparts energy, as well as the energies E_1 and E_2 , where $m_e c^2$ is the electron resting energy. In this study, the events were limited by the condition $E_1 + E_2$, shown in Section 2.5, and the Compton cone was drawn only for events in which the majority of the gamma-ray energy to be measured was imparted to the detector. By drawing multiple Compton cones, the overlap region can be obtained, and the direction in which the incident gamma rays flew can be identified.

$$\cos \theta = 1 - m_e c^2 \left(\frac{1}{E_2} - \frac{1}{E_1 + E_2} \right) \quad (1)$$

Owing to this principle, Compton cameras do not require shielding or the direction of the incident gamma rays to be specified in advance, as required by pinhole cameras. Therefore, they are advantageous in terms of miniaturization, weight reduction, and wide field of view.

2.1. Ce:GAGG Scintillator

Ce:GAGG ($\text{Ce}:\text{Gd}_3\text{Al}_2\text{Ga}_3\text{O}_{12}$ [11]) was used as the scintillator in the developed system. This scintillator is suitable for gamma-ray measurements owing to its large luminescence. In addition, a short decay time allows for a fast response. Furthermore, because it is not deliquescent and therefore does not deteriorate owing to moisture in the air, it can be used stably for long periods of time [12].

2.2. SiPM (Silicon Photomultiplier)

An SiPM (HAMAMATSU MPPC S13360-6025PE [13]) was adopted as the photodetector of the developed system. This device operates at low voltage and has the high

performance required for photon counting, including a high multiplication factor, fast response, excellent temporal resolution, and wide wavelength sensitivity. It also has the advantages of solid-state devices, such as being unaffected by magnetic fields and having shock resistance [14].

2.3. System Configuration

In this study, systems with a scintillator size of $10 \times 10 \times 10 \text{ mm}^3$ for a low dose rate and $4 \times 4 \times 4 \text{ mm}^3$ for a high dose rate were developed. By preparing scintillators of different sizes, measurements could be performed under appropriate conditions according to the dose rate of the measurement environment. Figure 3 shows a $4 \times 4 \times 4 \text{ mm}^3$ system [15]. The developed system comprises two sets of umbrella-like jigs with attached detectors: 32 for the scatterer and 32 for the absorber, totaling 64 detectors. This system can be opened and closed like an umbrella to change its shape, which yields the determination of the optimum sensitivity distribution when measuring the field of view. The umbrella angle (φ) is 0° when the umbrella is fully open and 90° when it is fully closed. The detector was fabricated by bonding a Ce:GAGG scintillator and an SiPM with a UV-curable optical adhesive, which was stored in an aluminum case. The light-transmission efficiency to the SiPM was increased by shielding all the surfaces of the Ce:GAGG scintillator with Teflon tape, except for the junction with the SiPM, to prevent the diffusion of the scintillation light. SiPMs with photosensitive areas of $6 \times 6 \text{ mm}^2$ were used in both systems. The center of one face of the Ce:GAGG scintillator was combined with the center of the photosensitive area of the SiPM. As shown in Figure 3b, the outer dimensions of the system are $38 \times 38 \times L \text{ cm}$ ($\varphi = 0^\circ$) and $10 \times 10 \times L + 14 \text{ cm}$ ($\varphi = 90^\circ$) when the distance between the scatterers and the absorbers is $L \text{ cm}$. However, it is possible to reduce the size by manufacturing a suitable jig for the detector arrangement and optimizing the sizes of the SiPM and the aluminum case of the $4 \times 4 \times 4 \text{ mm}^3$ system. Measurements using ^{137}Cs as the source at approximately 20°C resulted in an average detector energy resolution of approximately 6.5% for the $4 \times 4 \times 4 \text{ mm}^3$ system and 7.1% for the $10 \times 10 \times 10 \text{ mm}^3$ system.

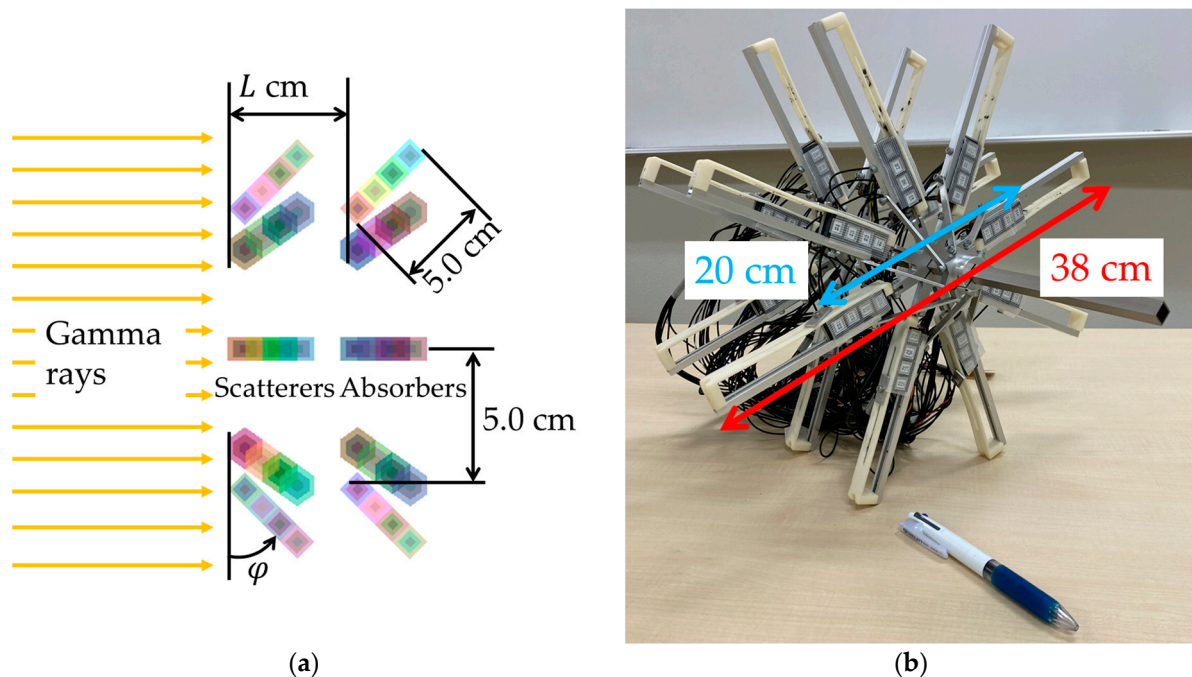


Figure 3. (a) Simulated measurement system with radiation transport calculation code EGS5 (Electron Gamma Shower Version 5) ($\varphi = 45^\circ$) [15]. (b) The actual measurement system ($\varphi = 0^\circ$). The distance L between the scatterers and the absorbers can be freely changed.

The signals output from the detectors are waveforms shaped by the head amplifier (CLEAR-PULSE Si-PM HEADAMP MODEL 80,364 [16]) and then transferred to an interface circuit (CLEAR-PULSE HEADAMP READOUT BOX MODEL 80389), where they are read by the software (LabVIEW 20.0.1). The time-constant CR for waveform shaping was set to $CR = 2.2 \mu\text{s}$ to make the decay time of Ce:GAGG negligibly long. In addition, the hold time of the waveform peak after waveform shaping was set to approximately $5 \mu\text{s}$. The software was used not only to visualize the direction of gamma rays in real time, but also to control the system, such as by adjusting the reverse voltage applied according to the ambient temperature to keep the SiPM multiplication factor constant. The reverse voltage applied to the SiPM was adjusted to between $54.7 \pm 3.0 \text{ V}$.

2.4. Output Method of Reconstructed Images

A Compton camera consists of a scatterer and an absorber, which makes it possible to draw more effective Compton cones when the source is on the scatterer side than when it is on the absorber side. Therefore, from the standpoint of measurement efficiency, it is important to have a scatterer on the side where the source resides. However, it is difficult to move or rotate a system in an environment where human access is restricted, such as inside a nuclear reactor building.

Because the developed system uses the same detector for both scatterers and absorbers, each of the 64 detectors can be programmed as either a scatterer or an absorber. This makes it possible to have a scatterer on the side where the source is located without changing the overall hardware system of the measurement device, which is expected to shorten measurement time. However, the position of the source is unknown at the start of the measurement, and the detector that should be set as the scatterer cannot be specified. Therefore, as shown in Figure 4, we set up the software to output two reconstructed images: one called “Frontview”, which is calculated by setting the 32 detectors on the front side of the system as scatterers and the others as absorbers, and the other called “Backview”, which is calculated by setting the 32 detectors on the back side of the system as scatterers and the others as absorbers. This allows us to acquire reconstructed images in all directions in real time, making it possible to perform measurements without losing measurement efficiency, even when the position of the source is unknown. The reconstructed image displays the source position in a Cartesian coordinate system, with the center of the system as the origin. The horizontal angle H and vertical angle V of the source as viewed from the system were defined as the horizontal and vertical axes, respectively.

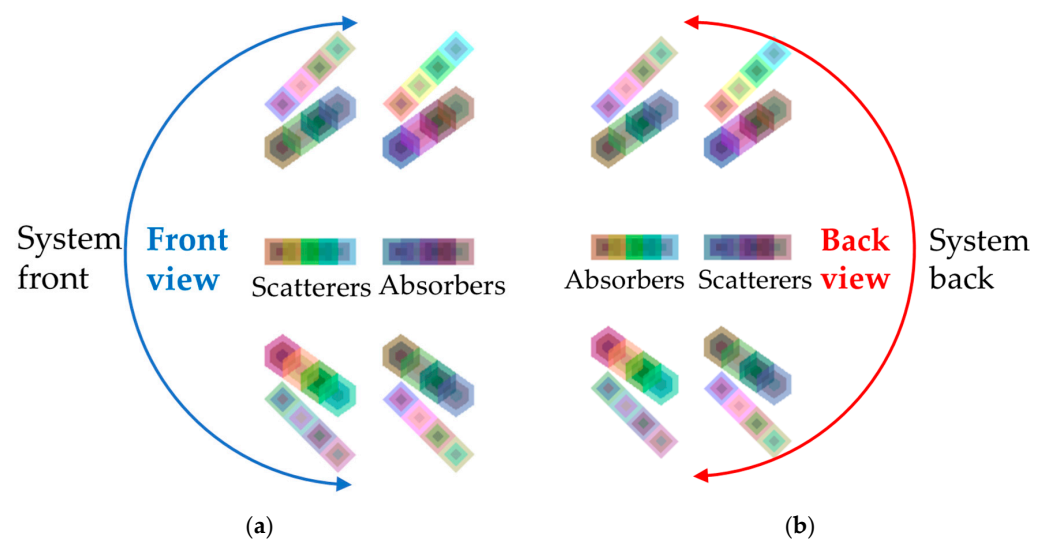


Figure 4. (a) Arrangement of scatterers and absorbers when outputting Frontview. (b) Arrangement of scatterers and absorbers when outputting Backview.

2.5. Drawing Conditions of the Compton Cone

The drawing conditions of the Compton cone were set as follows:

1. Considering the energy resolution of the Ce:GAGG scintillator used in the detector, an event was treated as valid when the sum of the energy E_1 given to the scatterer and the energy E_2 given to the absorber was within $\pm 5\%$ of the gamma-ray energy emitted from the objective nuclide. In the case of ^{137}Cs (662 keV), the event was treated as a valid event when the total energy of E_1 and E_2 ranged from 628.9 to 695.1 keV;
2. Owing to the structure of the system, when Compton scattering with a large scattering angle occurs in the scatterer, the scattered gamma rays hardly enter the absorbers to output a valid signal. Therefore, we only analyzed events with a scattering angle of 90° or less;
3. In some cases, incident gamma rays may cause multiple scattering with scatterers. To exclude such events, we assumed that the event was valid only when the energy was deposited in one scatterer and an absorber.

E_1 and E_2 were converted to 0 keV by the software if they were less than 20 keV to reduce the effect of noise.

3. Characterization of the $4 \times 4 \times 4 \text{ mm}^3$ System

3.1. Conditions of the Experiments and Simulations

We carried out an experiment to verify whether the $10 \times 10 \times 10 \text{ mm}^3$ system would work properly in low-dose-rate environments. In addition, a simulation was performed to evaluate the experimental results. Furthermore, we performed a simulation to calculate the measuring efficiencies (number of Compton cones to be drawn) by changing the umbrella angle φ and horizontal angle H . An experiment was also conducted to evaluate the maximum dose rate to which this system could be applied. The simulations were performed using EGS5 [17], which is a Monte Carlo simulation code that can analyze the transport phenomena of electrons, positrons, and photons in arbitrary elements, compounds, and mixtures. Simulations were performed using all physics calculation options set to default.

Table 1 lists the experimental and simulation conditions used. Figure 5 shows a schematic of the experiment and simulation in a low-dose-rate environment, In Figure 6, a simulation condition changing the umbrella angle φ is shown. Figure 7 depicts the experimental setup for the high-dose-rate environments. The source of radiation was ^{137}Cs , which is the main nuclide causing contamination in reactor buildings [2].

Table 1. Conditions of the experiments and simulations. The (a) 0° and (b) -45° of the high-dose-rate experiments correspond to Figure 7a,b.

	Low-Dose-Rate Experiment	Low-Dose-Rate Simulation	Simulation Changing the Umbrella Angle φ	High-Dose-Rate Experiments
Source	^{137}Cs Sealed source	^{137}Cs Point source	^{137}Cs Surface source	^{137}Cs Sealed source
Measurement time or number of gamma rays	40 h	22.8 billion (Isotropic source)	500 million (Parallel beams with 11 cm diameter)	20 min
Distance between the system center and the source D (Air dose rate at the center of the system)	100 cm (0.27 $\mu\text{Sv/h}$)	100 cm	-	350 cm (10 $\mu\text{Sv/h}$)
Umbrella angle φ	0°	0°	$0, 15, 30, 45, 60, 75, 90^\circ$	0°
Horizontal angle H of the source as viewed from the system	45°	45°	$0, \pm 30, \pm 60, \pm 90, \pm 120, \pm 150, 180 (-180)^\circ$	(a) 0° (b) -45°
Vertical angle V of the source as viewed from the system	0°	0°	0°	0°
Distance between scatterer and absorber L	5 cm	5 cm	5 cm	10 cm

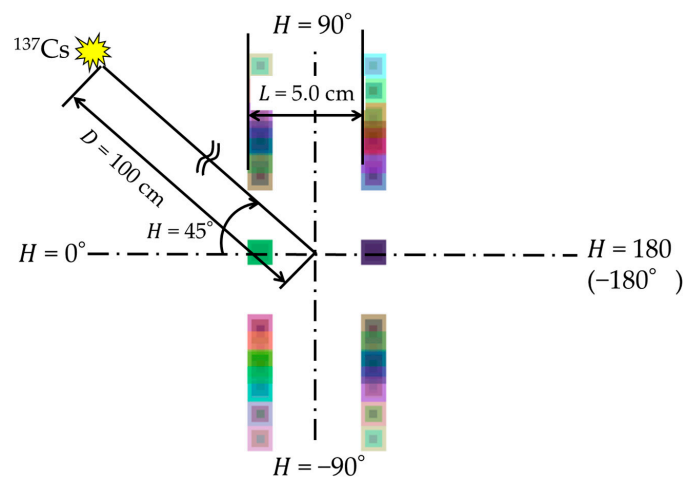


Figure 5. Bird's eye view of the measurement system used in low-dose-rate experiment and simulation.

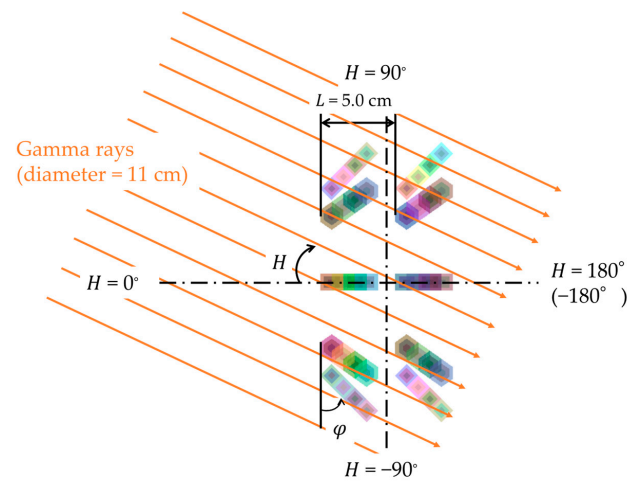
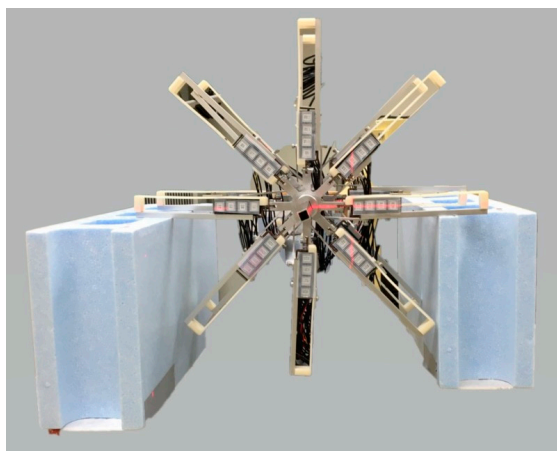


Figure 6. Bird's-eye view of the measurement system used in simulation where the umbrella angle φ is changed.



(a)



(b)

Figure 7. Photographs looking at the system from the source in high-dose-rate environment. The source was placed at (a) $H = 0^\circ, V = 0^\circ$ and (b) $H = -45^\circ, V = 0^\circ$ as viewed from the system.

3.2. Results of the Experiments and Simulations

3.2.1. Results of the Low-Dose-Rate Experiment and Simulation

Figure 8 shows the reconstructed images from the experiments and simulations at a low dose rate. It was confirmed that the developed $4 \times 4 \times 4 \text{ mm}^3$ system could visualize the incident direction of gamma rays. Table 2 lists the parameters of the reconstructed images. In this study, as shown in Figure 9a, we considered the average of the FWHMs obtained from the polynomial fitting of the data along dotted lines (1)–(4) centered at the estimated source position. The FWHM along dotted lines (1)–(4) was defined as FWHMs (1)–(4) and averaged. Figure 9b shows the results of the polynomial fitting using the least-squares method for the data along the dotted line (1).

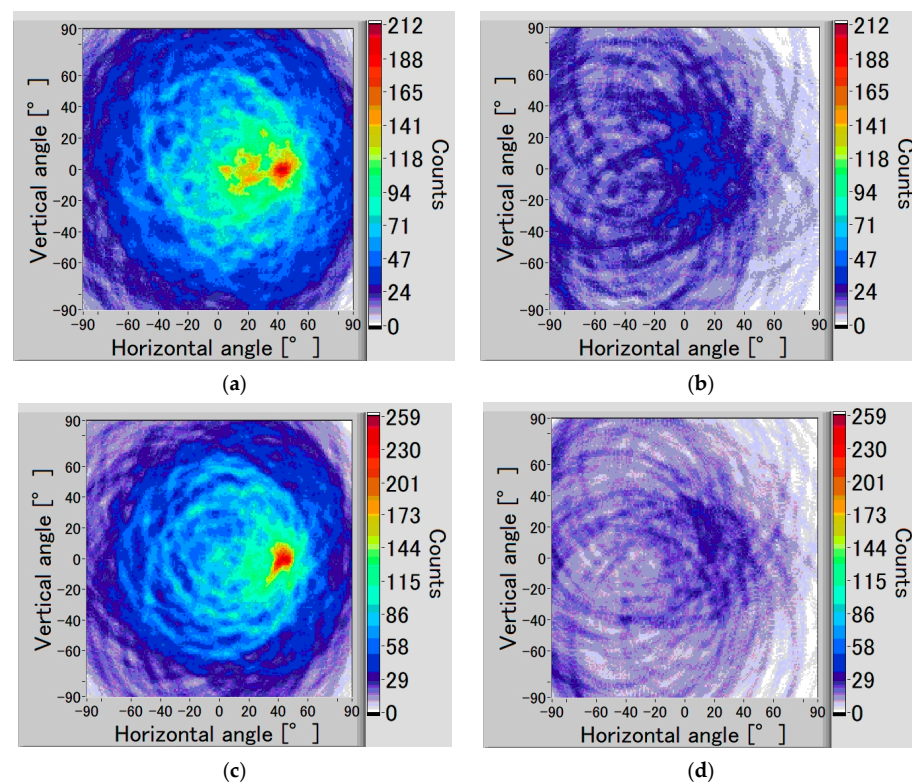


Figure 8. (a) Frontview and (b) Backview in low-dose-rate experiment and (c) Frontview and (d) Backview in a simulation for a low-dose-rate experiment, where the incident angle of gamma rays is all set to $H = 45^\circ$, $V = 0^\circ$, and the umbrella angle to be $\varphi = 0^\circ$. The width of the Compton cone was 2° .

The FWHM of the experimental results was larger than that of the simulation results. Although the cause of this has not been identified, it could be an accidental coincidence due to device noise. However, because there was no significant difference between the reconstructed images from the experiment and those from the simulation, the simulation can effectively evaluate the characteristics of this system in low-dose-rate regions.

Table 2. The parameters of the reconstructed images in the low-dose-rate experiment and simulation.

	(a)	(b)	(c)	(d)
FWHM at the estimated source position. (FWHM (1), FWHM (2), FWHM (3), FWHM (4))	27° ($31^\circ, 31^\circ, 21^\circ, 23^\circ$)	-	20° ($25^\circ, 18^\circ, 21^\circ, 16^\circ$)	-
H and V at the estimated source position.	$H = 44^\circ$, $V = 0^\circ$	-	$H = 44^\circ$, $V = 0^\circ$	-
Number of events (Compton cones).	1363 counts	454 counts	1363 counts	364 counts

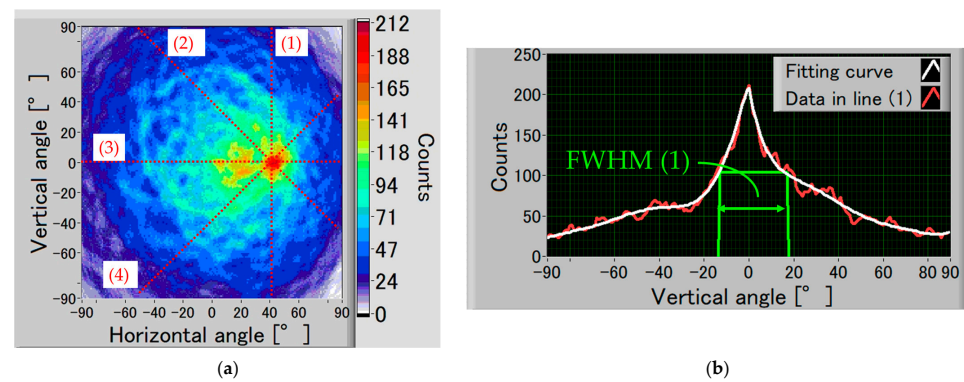


Figure 9. (a) Schematic view of the analysis in Figure 8a. FWHM was evaluated by fitting the data along the dotted lines (1)–(4). The center coordinate of the dotted line is the estimated source position ($H = 44^\circ$, $V = 0^\circ$). (b) Results of polynomial fitting using the least-squares method to the data along the dotted line (1). The FWHM (1) was 31° .

3.2.2. Result of Simulation with Changing the Umbrella Angle φ

Figure 10 shows the distribution of the calculated number of events normalized by the umbrella angle $\varphi = 0^\circ$, where the vertical and horizontal angles were set to $H = 0^\circ$ and $V = 0^\circ$. The distance from the origin represents the number of events in each plot. When $H = 0^\circ$ to $\pm 30^\circ$ or $H = \pm 150^\circ$ to 180° (-180°), the results with $\varphi = 0^\circ$ showed the highest efficiency (red graph). On the other hand, when H takes other values than those mentioned above, the data with $\varphi = 90^\circ$ were the highest (blue graph). This indicates that by changing the value of φ , the developed system can achieve a nearly uniform efficiency distribution in all directions.

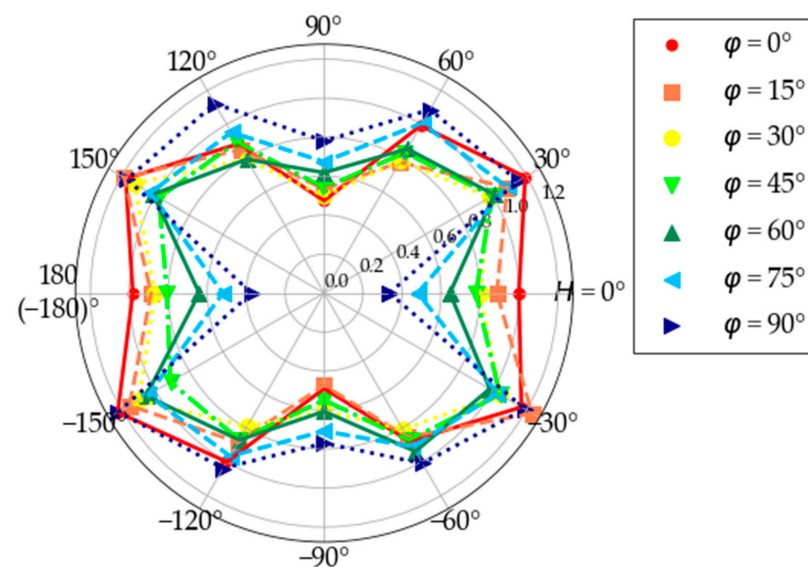


Figure 10. Distribution of the number of normalized events.

3.2.3. Results of the High-Dose-Rate Experiment

Figure 11 shows the reconstructed images in the high-dose-rate experiment, where the direction of the incoming gamma rays was visualized at an air dose rate of $10 \mu\text{Sv/h}$. Table 3 lists each parameter of the reconstructed images. Compared to the results of the low-dose-rate experiment, the FWHM of the Frontview increased, and the counts in the Backview increased. Although the cause of this was not identified, the number of accidental coincidences owing to different gamma rays may have been higher at lower dose rates.

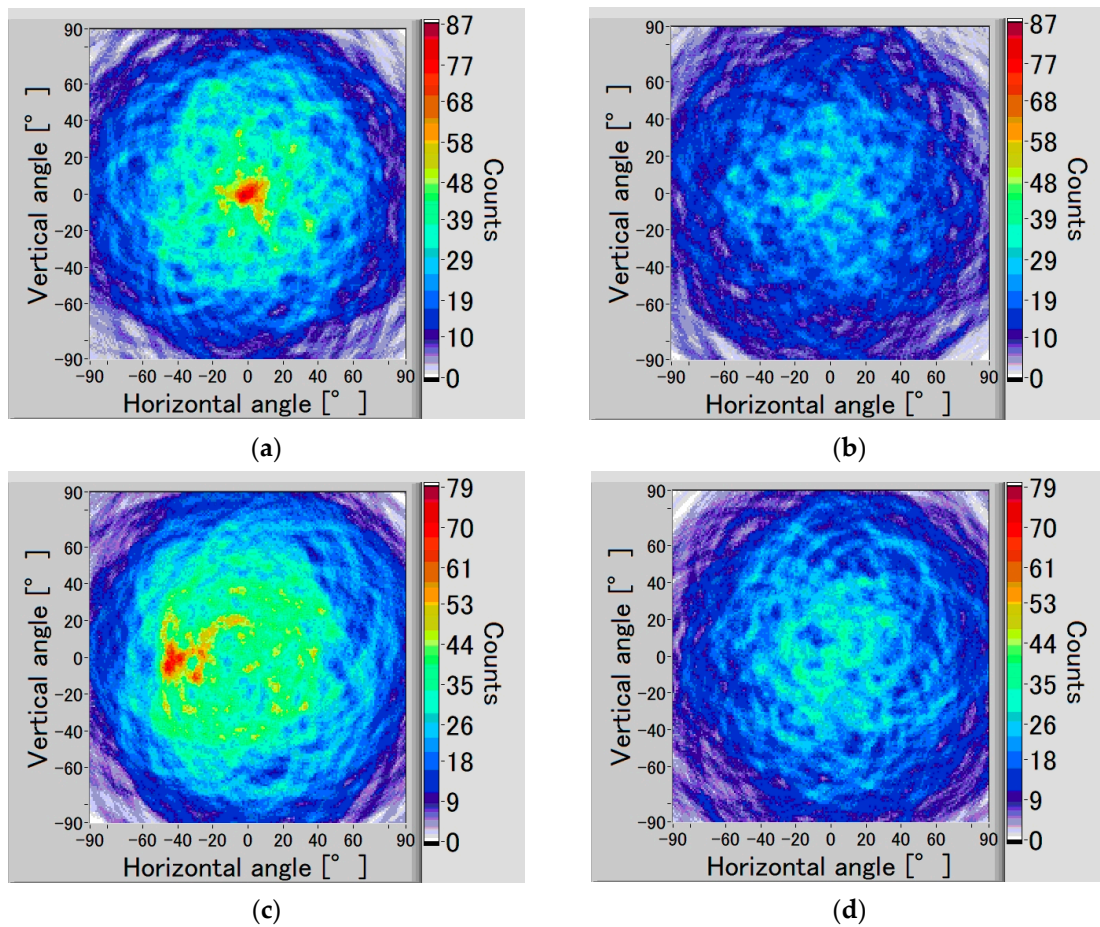


Figure 11. (a) Frontview and (b) Backview with the source located at $H = 0^\circ, V = 0^\circ$; (c) Frontview and (d) Backview with the source located at $H = -45^\circ, V = 0^\circ$.

Table 3. The parameters of the reconstructed images in the high-dose-rate experiment.

	(a)	(b)	(c)	(d)
FWHM at the estimated source position. (FWHM (1), FWHM (2), FWHM (3), FWHM (4))	26° (19°, 29°, 32°, 22°)	-	46° (67°, 30°, 37°, 50°)	-
H and V at the estimated source position.	$H = -3^\circ,$ $V = -2^\circ$	-	$H = -46^\circ,$ $V = -6^\circ$	-
Number of events (Compton cones).	590 counts	414 counts	610 counts	430 counts

On the other hand, in high-dose-rate experiments exceeding 10 $\mu\text{Sv/h}$, measurement was not possible owing to software outage.

4. Improvements in Software

4.1. Improvements in Software for Faster Data Loading

In high-dose-rate experiments, as too many events occur at both scatterers and absorbers, the data-loading speed of the software is not sufficient to process them properly. Therefore, we improved the software to increase the data-loading speed using the following techniques:

1. A data structure called a queue was used to exchange data within the software. Before the improvement, the software used a queue between the loop for reading data and the loop for analyzing the read data. However, a queue temporarily stores data in the

- storage area (memory), which reduces the analysis speed. Therefore, we improved the program structure by eliminating the use of queues;
2. To reduce the amount of data to be analyzed, we stopped displaying all pulse-height distributions for the 64 detectors. After the improvement, the software displayed the pulse-height distributions only for selected detectors;
 3. As shown in Figure 12a, before the improvement, a virtual COM port was used for data transmission between the extension buffer and the software. However, the virtual COM port is a bottleneck owing to its slow data-read speed. Therefore, a DLL program based on C was created to achieve data I/O without a virtual COM port. After the improvement, as shown in Figure 12b, data were transferred without using the COM port by executing a DLL program in the software;
 4. Before the improvement, the software read and analyzed all event data. However, after the improvement, the software could freely change the frequency of data transmission in the extension buffer. This enabled adjusting the amount of event data to be read according to the air dose rate, thus allowing more leeway for data analysis.

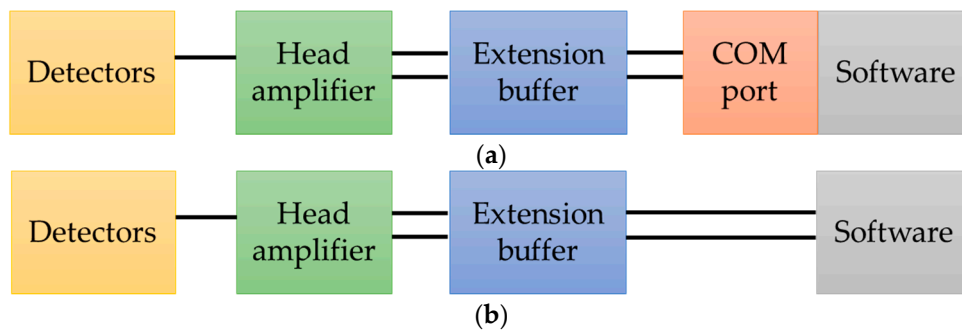


Figure 12. (a) Data structure of the system before improvement. (b) Data structure of the system after improvement.

4.2. Result of Software Improvements

Table 4 shows the dose rate limits at which the system can read data without stopping before and after the software improvements. Although the limit could not be measured for the $10 \times 10 \times 10 \text{ mm}^3$ system owing to insufficient gamma-ray source strength, the improved system was confirmed to be able to work at least at $255 \text{ } \mu\text{Sv/h}$. This value was approximately 268 times higher than that achieved before the improvement. If we assume that the same improvement can be realized for the $4 \times 4 \times 4 \text{ mm}^3$ system, it is expected to be able to work at approximately 2.68 mSv/h . Furthermore, based on the expectations that (1) a $10 \times 10 \times 10 \text{ mm}^3$ system can operate at $255 \text{ } \mu\text{Sv/h}$ or higher and (2) the lower counting rate of the $4 \times 4 \times 4 \text{ mm}^3$ system, the actual dose-rate limit for the $4 \times 4 \times 4 \text{ mm}^3$ system may be higher than 2.68 mSv/h .

Table 4. The dose rate limits at which the system can read data before and after the improvements.

	$10 \times 10 \times 10 \text{ mm}^3$ System	$4 \times 4 \times 4 \text{ mm}^3$ System
Before improvements	$0.95 \text{ } \mu\text{Sv/h}$ (Experimental value)	$10 \text{ } \mu\text{Sv/h}$ (Experimental value)
After improvements	$255 \text{ } \mu\text{Sv/h}$ (Experimental value: Maximum air dose rate that could be produced by the gamma source used in the experiment.)	2.68 mSv/h (Estimated from the results of calculation)

Future experiments using a stronger source are necessary to confirm the limit of the $10 \times 10 \times 10 \text{ mm}^3$ system. In addition, we evaluate whether the system can be applied to the environment inside a reactor building. If it is difficult to apply the system, hardware improvements, such as changes in the scintillator size, should be considered.

5. Shifting Phenomenon of Pulse-Height Distribution

On the other hand, as shown in Figure 13, under high-dose-rate conditions, the pulse-height distribution shifted to the lower energy side for the 10 mm square system. Figure 13a shows the relationship between the air dose rate and the pulse height (ch) of the photoelectric peak. The magnitude of the shift increased as the dose rate increased. This phenomenon affects Compton cone drawing because it makes accurate conversion from ch to energy (E_g) difficult. Figure 13b shows the pulse-height distributions measured in environments with different dose rates. In the pulse-height distribution at 2.35 mSv/h, the counts were also higher on the right side of the peak owing to pile-up. However, because the pile-up cannot explain the shift to the lower energy side in a high counting rate environment, the direct cause of the shifting phenomenon must be other than the pile-up itself, as discussed in Sections 5.1 and 5.2. In addition, the $4 \times 4 \times 4 \text{ mm}^3$ system has a lower probability of the shifting phenomenon than the $10 \times 10 \times 10 \text{ mm}^3$ system, but it may occur in high-dose-rate regions.

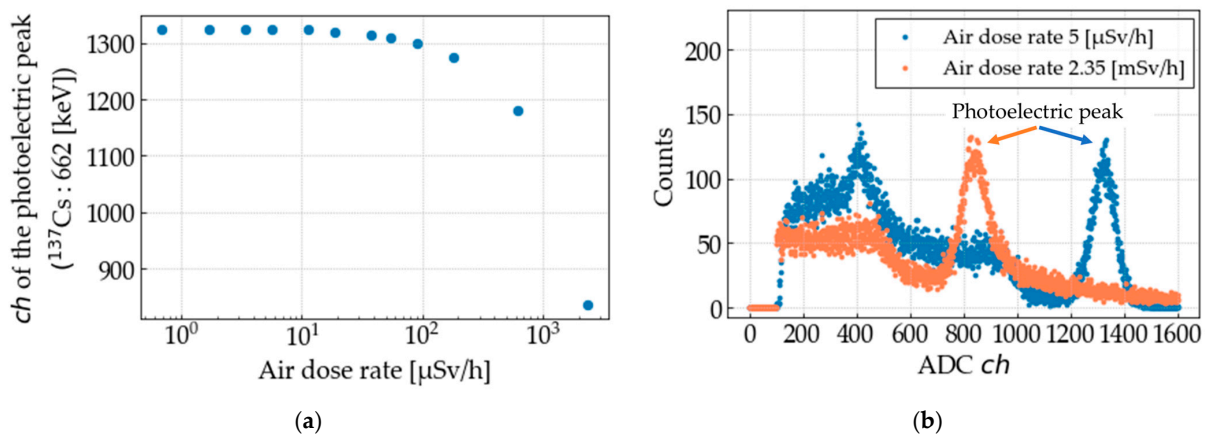


Figure 13. (a) Relationship between air dose rate and the ch of the photoelectric peak. (b) Shift in pulse-height distribution with increasing air dose rate.

5.1. Hardware Survey and Results to Address the Shifting Phenomenon

At a high dose rate, the HV current (I_{HV}) flowing through the SiPM increases, resulting in a larger voltage drop across the filter resistor and a decrease in the voltage applied to the SiPM is expected [14]. To reduce the voltage drop, the filter resistor was changed from 1 k Ω to 100 Ω in the circuit used for the system shown in Figure 14a, but no effect was observed. Therefore, it was found that the voltage drop in the resistor was not the direct cause of the shifting phenomenon.

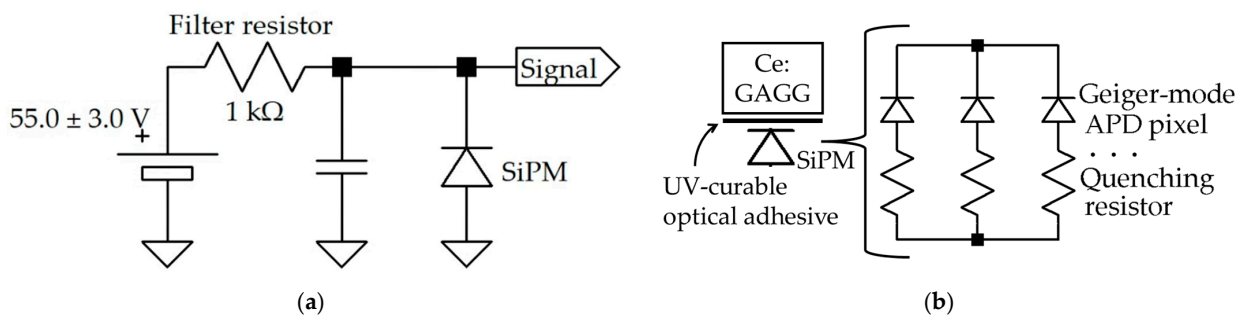


Figure 14. (a) Circuit of SiPM [14]. (b) Structure of SiPM [14].

Another cause is thought to be the performance bottleneck of the SiPM. As shown in Figure 14b, the SiPM has a structure in which avalanche photodiode (APD) pixels operating in Geiger mode are connected in parallel. The charges contained in all pulses were summed

and outputted. However, because the Geiger-mode APD pixels must be recharged after output, they become insensitive during this time [14]. Therefore, as the dose rate increases, the number of pixels that can output the signal decreases. A possible countermeasure to this problem is to change the SiPMs to models with a larger number of pixels and a shorter insensitivity time. However, because SiPMs with relatively high performance have already been in use, significant improvement is not expected.

5.2. Software Improvement and the Results

To reduce the errors caused by the shifting phenomenon using software, we developed a new correction technique for software control. Equation (2) is the energy calibration formula, assuming a linear relationship between the digitally converted pulse height ch and gamma-ray energy E_g . Under low-dose-rate conditions, the values of A can be assumed to be constant. However, under a high dose rate, as A changed depending on the dose rate, we attempted to correct the values of A based on the monitored current values from the high-voltage source: I_{HV} .

$$E_g = A \cdot ch + B \tag{2}$$

For the $10 \times 10 \times 10 \text{ mm}^3$ system shown in Figure 15, the relationship between ch of the photoelectric peak and I_{HV} for one detector was investigated. In addition, eight detectors were placed at a uniform distance from the gamma-ray source, and I_{HV} was measured by changing the number of detectors ($N_{detector}$) by removing one detector at a time.

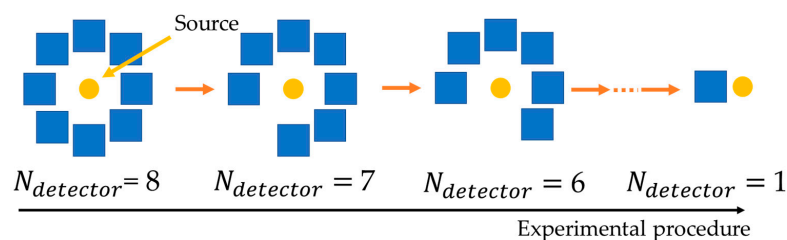


Figure 15. System of experiments using multiple detectors.

Figure 16a illustrates the relationship between I_{HV} and ch . It shows that both the peak shift and I_{HV} increase when many pixels simultaneously output signals in the SiPM. Although the reason for these linear relationships cannot be explained currently, a linear relationship was observed. Figure 16b depicts the dependency of I_{HV} on $N_{detector}$, where I_{HV} increases linearly with $N_{detector}$. We introduced these relationships into the software for energy calibration based on Equation (3), where I_{HV0} and ch_0 are I_{HV} and ch are in the background, respectively, and C is the slope of the linear function in Figure 16a.

$$E_g = \frac{A \cdot ch_0 \cdot ch}{ch_0 + \frac{(I_{HV} - I_{HV0})C}{N_{detector}}} + B \tag{3}$$

As shown in Figure 17a, we used 32 detectors in a $10 \times 10 \times 10 \text{ mm}^3$ system to demonstrate the correction technique mentioned above ($N_{detector} = 32$). Figure 17b shows the energy spectra before and after the correction. The results demonstrate that the correction technique can successfully reduce the shifting phenomenon. Furthermore, because this correction method was used to measure I_{HV} under the air dose rate at each time point, it is expected to be applicable in environments where the air dose rate changes, such as when mounted on a robot.

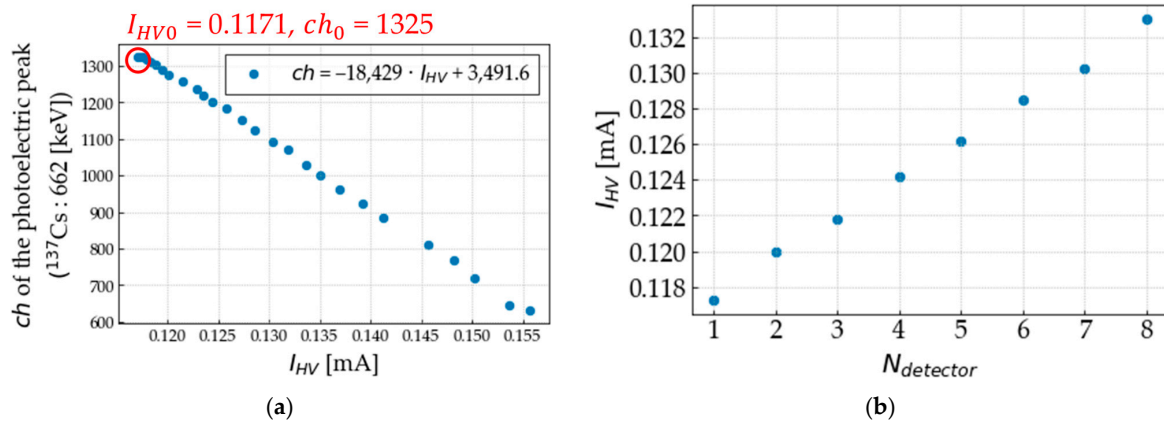


Figure 16. (a) Relationship between I_{HV} and ch of photoelectric peak for one detector. (b) Relationship between $N_{detector}$ and I_{HV} .

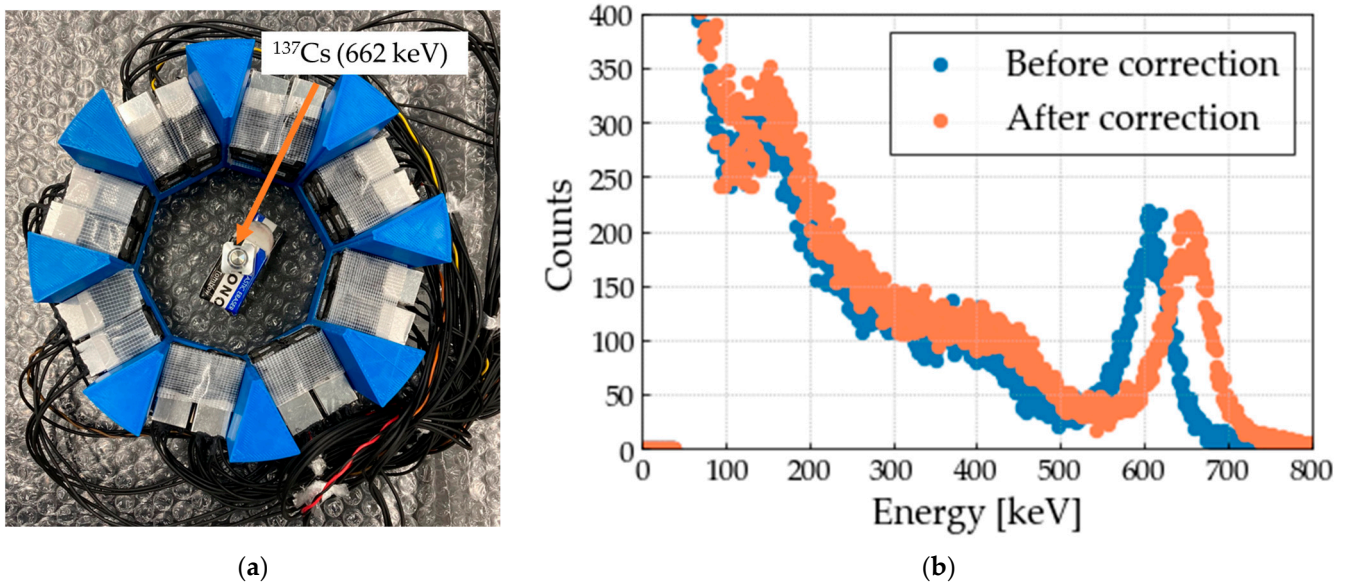


Figure 17. (a) Each detector was 5 cm away from the source (^{137}Cs : 662 keV), and the air dose rate was approximately $223 \mu\text{Sv/h}$. (b) Energy spectra before and after correction. Before correction, the energy of the photoelectric peak has shifted to the low energy side at 600 keV, but after correction, it appears around 662 keV.

6. Conclusions

Through experiments and simulations, we characterized an umbrella-shaped Compton camera developed for application in a high-dose-rate environment inside a nuclear reactor building at the Fukushima Daiichi Nuclear Power Station. The detectors for this system are $4 \times 4 \times 4 \text{ mm}^3$ Ce:GAGG and SiPM, which are capable of fast response. Simulations were performed, which demonstrated that by changing the umbrella angle φ , the developed system can achieve a nearly uniform efficiency distribution in all directions. Without the improvements in the control software, the system has been shown to be able to be applied to environments up to $10 \mu\text{Sv/h}$. By improvements in data-loading speed, we were able to increase the applicable dosage rate by a factor of at least 268. We calculated that the system is applicable to approximately 2.68 mSv/h . On the other hand, we observed that the pulse-height distribution shifted with an increasing dose rate. We succeeded in reducing the effect of the shift using a correction technique in the energy calibration formula. We plan to investigate the exact limits of the applicable dose rate of the system in future experiments using more intensive gamma radiation sources. Furthermore, it is necessary to

appropriately select the dose rate range for which the $10 \times 10 \times 10 \text{ mm}^3$ system should be used, as well as address the adhesion of radioactive substances to the detector and damage to the SiPM in radioactive environments.

Author Contributions: Conceptualization, K.M., E.T. and Y.S.; methodology, K.M. and E.T.; software, K.M.; formal analysis, K.M. and E.T.; investigation, E.T. and Y.S.; resources, Y.S.; data curation, K.M.; writing—original draft, K.M.; writing—review and editing, E.T. and Y.S.; visualization, K.M.; supervision, E.T.; project administration, E.T. and Y.S.; funding acquisition, Y.S. All authors have read and agreed to the published version of the manuscript.

Funding: This study was funded by [JSPS (Japan Society for the Promotion of Science)] KAKENHI grant number [JP19K15484] and the APC was funded by [National Institute of Technology (KOSEN), Japan].

Conflicts of Interest: The authors declare no conflict of interest.

References

1. Tokyo Electric Power Company, Inc. Fukushima Nuclear Accident Analysis Report. Available online: https://www4.tepco.co.jp/en/press/corp-com/release/betu12_e/images/120620e0104.pdf (accessed on 9 March 2023).
2. Dohi, T.; Ohmura, Y.; Kashiwadani, H.; Fujiwara, K.; Sakamoto, Y.; Iijima, K. Radiocaesium activity concentrations in parmelioid lichens within a 60 km radius of the Fukushima Dai-ichi Nuclear Power Plant. *J. Environ. Radioact.* **2015**, *146*, 125–133. [[CrossRef](#)] [[PubMed](#)]
3. Okada, K.; Tadokoro, T.; Ueno, Y.; Nukaga, J.; Ishitsu, T.; Takahashi, I.; Fujishima, Y.; Hayashi, K.; Nagashima, K. Development of a gamma camera to image radiation fields. *Prog. Nucl. Sci. Technol.* **2014**, *4*, 14–17. [[CrossRef](#)]
4. Ueno, Y.; Takahashi, I.; Ishitsu, T.; Tadokoro, T.; Okada, K.; Nagumo, Y.; Fujishima, Y.; Kometani, Y.; Suzuki, Y.; Umegaki, K. Spectroscopic gamma camera for use in high dose environments. *Nucl. Instrum. Methods Phys. Res.* **2016**, *822*, 48–56. [[CrossRef](#)]
5. Mizuno, T.; Arimoto, M.; Sato, D.; Yoshiura, K.; Tomoda, T.; Ishiguro, K.; Kataoka, J.; Sawano, T.; Yonetoku, D.; Terazawa, S.; et al. Development of an MPPC-based gamma-ray detector onboard a radiation source imager under high-dose environments and initial performance results. *Nucl. Instrum. Methods Phys. Res.* **2023**, *1046*, 167544. [[CrossRef](#)]
6. Sueoka, K.; Kataoka, J.; Takabe, M.; Iwamoto, Y.; Arimoto, M.; Yoneyama, M.; Yoda, I.; Torii, T.; Sato, Y.; Kaburagi, M.; et al. Development of a new pinhole camera for imaging in high dose-rate environments. *Nucl. Instrum. Methods Phys. Res.* **2018**, *912*, 115–118. [[CrossRef](#)]
7. Kataoka, J.; Kishimoto, A.; Nishiyama, T.; Fujita, T.; Takeuchi, K.; Kato, T.; Nakamori, T.; Ohsuka, S.; Nakamura, S.; Hirayanagi, M.; et al. Handy Compton camera using 3D position-sensitive scintillators coupled with large-area monolithic MPPC arrays. *Nucl. Instrum. Methods Phys. Res.* **2013**, *732*, 403–407. [[CrossRef](#)]
8. Sato, Y.; Terasaka, Y. Radiation imaging using an integrated Radiation Imaging System based on a compact Compton camera under unit 1/2 exhaust stack of Fukushima Daiichi Nuclear Power Station. *J. Nucl. Sci. Technol.* **2022**, *59*, 677–687. [[CrossRef](#)]
9. Sato, Y.; Terasaka, Y.; Terasaka, Y.; Usami, H.; Kaburagi, M.; Kawabata, K.; Utsugi, W.; Kikuchi, H.; Takahira, S.; Torii, T. Radiation imaging using a compact Compton camera inside the Fukushima Daiichi Nuclear Power Station building. *J. Nucl. Sci. Technol.* **2018**, *55*, 9. [[CrossRef](#)]
10. Schönfelder, V.; Hirner, A.; Schneider, K. A telescope for soft gamma ray astronomy. *Nucl. Instrum. Methods* **1973**, *107*, 385–394. [[CrossRef](#)]
11. Kamada, K.; Yanagida, T.; Endo, T.; Tsutumi, K.; Usuki, Y.; Nikl, M.; Fujimoto, Y.; Fukabori, A.; Yoshikawa, A. 2 inch diameter single crystal growth and scintillation properties of Ce:Gd₃Al₂Ga₃O₁₂. *J. Cryst. Growth* **2012**, *352*, 88–90. [[CrossRef](#)]
12. Yeom, J.Y.; Yamamoto, S.; Derenzo, S.E.; Spanoudaki, V.C.; Kamada, K.; Endo, T.; Levin, C.S. First Performance Results of Ce:GAGG Scintillation Crystals With Silicon Photomultipliers. *IEEE Trans. Nucl. Sci.* **2013**, *60*, 988–922. [[CrossRef](#)]
13. Hamamatsu Photonics K.K. Product Information/MPPC. Available online: https://www.hamamatsu.com/content/dam/hamamatsu-photonics/sites/documents/99_SALES_LIBRARY/ssd/mppc_kapd0006e.pdf (accessed on 11 March 2023).
14. Hamamatsu Photonics K.K. Technical Note/MPPC. Available online: https://www.hamamatsu.com/content/dam/hamamatsu-photonics/sites/documents/99_SALES_LIBRARY/ssd/mppc_kapd9008e.pdf (accessed on 11 March 2023).
15. Miyada, K.; Takada, E.; Sato, Y. Application of Shape-Variable Gamma Camera to High Dose Rate Regions. In Proceedings of the 1st KOSEN Research International Symposium (KRIS2023), Hitotsubashi Hall, Tokyo, Japan, 1–2 March 2023.

16. CLEAR-PULSE, SiPM-yō Heddoanpuyunitto 80364-Gata. Available online: https://clearpulse.co.jp/pdf/80364_catalog.pdf (accessed on 11 March 2023). (In Japanese).
17. Hirayama, H.; Namito, Y.; Bielajew, A.F. *The EGS5 Code System*; SLAC-R-730 and KEK Report 2005-8; US Department of Energy: Washington, DC, USA, 2005.

Disclaimer/Publisher's Note: The statements, opinions and data contained in all publications are solely those of the individual author(s) and contributor(s) and not of MDPI and/or the editor(s). MDPI and/or the editor(s) disclaim responsibility for any injury to people or property resulting from any ideas, methods, instructions or products referred to in the content.